A halide methyltransferase family unites methyl-donor regeneration and methylation in a single scaffold

Junxi Chi[1,2,3,#], Peishan Li[4,#], Shaixiao Tian[5,#], Zhi-Min Zhang*[4], Jian-bo Wang*[1,2,3,5]

[1]Department of Microbiology, Zhejiang University School of Medicine, Hangzhou, 310058, P. R. China. [2]Key Laboratory of Multiple Organ Failure (Zhejiang University), Ministry of Education, Department of General Intensive Care Unit of the Second Affiliated Hospital (Zhejiang University), Zhejiang University School of Medicine, Hangzhou, 310058, P. R. China. [3]Institute of Pharmaceutical Biotechnology Zhejiang University School of Medicine, Hangzhou, 310058, P. R. China. [4]State Key Laboratory of Bioactive Molecules and Draggability Assessment, Jinan University, Guangzhou, 511436, P. R. China. [5]Key Laboratory of Chemical Biology and Traditional Chinese Medicine Research (Ministry of Education) and Key Laboratory of Phytochemistry R&D of Hunan Province, College of Chemistry and Chemical Engineering, Hunan Normal University, Changsha, 410081, P. R. China.

[#]These authors contributed equally: Junxi Chi, Peishan Li, and Shaixiao Tian.

***Correspondence:** jwang2023@zju.edu.cn; zhangzm@jnu.edu.cn

Abstract

The “magic methyl effect” is central to drug discovery, yet achieving precise methylation remains challenging. Methyltransferases offer high selectivity but are limited by inefficient methyl-donor regeneration. Halide methyltransferases (HMTs) in multienzyme cascades expand donor scope but suffer from complexity, cost, and poor inter-enzyme mass transfer. Here we report for the first time a halide methyltransferase from *Aspergillus terreus* (*Ate*HMT) that directly couples methyl-donor regeneration with substrate methylation within a single enzyme using methyl iodide. Directed evolution enhances this noncanonical activity by ~100-fold. Structural analysis of donor–acceptor–enzyme complexes reveals that substrate-induced N-terminal loop reorganization enables productive acceptor binding and catalytic coupling. We further demonstrate that this bifunctionality is conserved across an HMT subfamily via sequence similarity network analysis and mutagenesis. Engineered variants enable efficient methylation of diverse substrates, establishing a general single-enzyme platform. This work efficiently collapses methyl-donor supply and transfer into one polypeptide, overcoming a long-standing limitation in biocatalytic methylation.

INTRODUCTION

The so-called magic methyl effect can profoundly enhance the functional value of bioactive molecules[1], as the installation of a single methyl group often induces disproportionate changes in biological activity. Especially in therapeutic settings, methylation can increase lipophilicity, enhance metabolic stability, and improve target potency, collectively leading to superior bioavailability[2]. Although a wide range of chemical methylation strategies—using reagents such as dimethyl carbonate or methyl iodide—have been developed, achieving precise regio- and chemoselectivity across complex molecular scaffolds remains challenging[3,4]. In contrast, enzymatic methylation has emerged as a powerful alternative, offering unparalleled selectivity through well-defined active-site architectures and substrate recognition mechanisms[5-7], thereby providing a compelling platform for controlled and sustainable methyl group installation.

Although *S*-adenosyl-L-methionine (SAM)–dependent methyltransferases catalyze a wide range of highly selective methylation reactions—including site-specific modification of C, O, N, and S atoms[8-14]—their broader application is constrained by the high cost of SAM and inefficient cofactor regeneration[15]. The discovery of halide methyltransferases (HMTs) in 2019 provided a potential solution to these limitations by enabling SAM regeneration through methyl transfer from halogenated alkanes to *S*-adenosyl-L-homocysteine (SAH)[16], thereby substantially improving atom economy. Owing to their broad substrate tolerance and high catalytic efficiency, HMTs can function cooperatively with SAM-dependent methyltransferases to support sustained methylation processes[17-19]. Indeed, dual-methyltransferase cascade systems incorporating HMTs have been successfully applied to a range of alkylation reactions[20-23]. However, such systems require careful orchestration of enzyme ratios and reaction conditions to achieve high efficiency, and they remain inherently burdened by increased operational complexity and inter-enzyme mass-transfer limitations. Consequently, eliminating these barriers—particularly those associated with cost and material transfer—remains essential for the practical deployment of biocatalytic methylation technologies.

Beyond multi-enzyme coupling strategies, substrate-coupling biocatalytic systems provide an alternative paradigm in which a single enzyme catalyzes two or more sequential steps within a cascade reaction. In such systems, a single biocatalyst simultaneously accomplishes cofactor regeneration and target product formation, thereby minimizing operational complexity and mass-transfer limitations. Substrate-coupling strategies have been successfully implemented with dehydrogenases and glycosyltransferases[24,25], and our previous work demonstrated a glucose dehydrogenase–based substrate-coupling system for asymmetric synthesis[26]. However, no analogous system has been reported for methyltransferases.

To overcome the cost inefficiency and operational complexity of conventional dual-methyltransferase systems (Fig. 1a), we report a bifunctional catalytic mode in which a single halide methyltransferase unites

methyl-donor regeneration and substrate methylation (Fig. 1b). Through enzyme mining and rational engineering, we identify an HMT with intrinsic substrate-coupling activity and further enhance its catalytic performance. Structural and mechanistic analyses elucidate the molecular basis of this unconventional reactivity. The engineered system enables efficient methylation of diverse substrates, demonstrating its synthetic utility. Moreover, the identification of additional HMTs with similar activity indicates that this functionality is not unique to a single enzyme. Together, these findings establish a streamlined and efficient framework for biocatalytic methylation and define a new paradigm for the application of halide methyltransferases in synthesis.

RESULTS & DISCUSSION

Intrinsic substrate-coupled methylation activity in halide methyltransferases

Inspired by previously reported substrate-coupling enzymatic systems, we hypothesized that halide methyltransferases with broad substrate scope might also possess the ability to transfer a methyl group to substrates other than halide ions. Based on this assumption, we evaluated in-house halide methyltransferases that was used to construct classical cascade reactions by coupling halide methyltransferases with major methyltransferases in other projects. Two representative acceptors—2,7-dihydroxynaphthalene (**1A**) and kaempferol (**1a**)—were employed as molecular probes, together with SAH and methyl iodide, to screen candidate HMTs.

Six HMTs (*Ate*HMT from *Aspergillus terreus*, *Ap*HMT from *Aspergillus pseudoviridinutans*, *Ath*HMT from *Aspergillus thermomutatus*, *Ana*HMT from *Aspergillus nanangensis*, *Pp*HMT from *Penicillium polonicum*, and *Sg*HMT from *Sporisorium graminicola*), synthesized in a parallel project and highly homologous to the known broad-substrate-spectrum enzyme *Acl*HMT[27], were tested. All reaction assays were analyzed by high-performance liquid chromatography (HPLC) and LC–MS. The results indicated that *Ate*HMT exhibited low but discernible activity, with monomethylated products detected for both **1A** (conversion: 2.54%) and **1a** (conversion: 0.45%). By comparison with commercial standards, both products

2A and **2a** were identified as the 7-*O*-methylated derivatives of **1A** and **1a**, respectively (Fig. S1-2 and Tab. S6).

These findings imply that halide methyltransferases may harbor an intrinsic capacity to catalyze methylation reactions autonomously, without reliance on elaborate multi-enzyme cascade architectures.

Structure-guided engineering of *Ate*HMT

Because the activity of wild-type *Ate*HMT (*Ate*HMT-WT) toward the model substrates was relatively weak, directed evolution[28-33] was performed to enhance catalytic reactivity and to identify key residues involved in regulating activity and selectivity. As *Ate*HMT exhibited activity toward both **1A** and **1a**, independent directed evolution strategies were conducted separately for each substrate.

To provide a reliable structural framework for enzyme engineering, we determined the crystal structure of the *Ate*HMT–SAH complex at a resolution of 1.80 Å (Fig S3a). The polypeptide backbone was well defined, except for the first four residues of the N-terminal loop (loop1). Clear residual electron density in the active site was confidently modeled as SAH and a glycerol molecule, the latter originating from the cryoprotectant used during crystal harvesting. The bound SAH is shielded by a loop comprising residues 38–45 (loop2). Together, loop1 and loop2 constitute the active-site loops. Exploration of alternative conformations of these loops is expected to expand the substrate-binding pocket and enhance substrate promiscuity[34]. A Dali structural homology search revealed that *Ate*HMT shares the highest similarity with the recently characterized halide methyltransferase KIO from *E. coli*[35], with a backbone r.m.s. deviation of 2.40 Å over 235 residues (Fig. S3b). In addition to the conserved Rossmann-type core fold and SAH-binding mode common to halide methyltransferases, *Ate*HMT contains two distinctive structural features: a protruding antiparallel β-sheet (residues 64–74) and an unusually long loop (residues 223–248) that closely adheres to the surface of the Rossmann core (Fig. S3b-3d). The biological role of these elements remains elusive.

For substrate **1A**, with the high-resolution structure in hand and considering that the acceptor substrate likely shares the same active site as methyl iodide but is substantially larger in volume, we hypothesized that the substrate-access tunnel would be a critical determinant of catalytic efficiency. Accordingly, CAVER 3.0.3[36] was used to identify the entry pathway for methyl iodide, and amino acid residues within a 5 Å range

of this pathway—including P210, W40, C167, R200, T164, F198, and A168—were targeted (Fig. S4a-b). Alanine scanning mutagenesis was employed to identify mutational "hotspots" at the bottleneck region of the substrate access channel. Product formation was quantified by HPLC, revealing that the *Ate*HMT-C167A mutant exhibited substantially enhanced catalytic efficiency, approximately 16-fold higher than that of the wild-type enzyme.

Subsequently, to further optimize single-enzyme methylation activity toward substrate **1A**, we docked **1A** into the active pocket and performed site-saturation mutagenesis (SSM)[31,37-40] on 13 residues located within a 5 Å radius of the docked **1A** molecule: C167, A168, W27, M11, P39, W40, L38, V264, T164, P209, P210, R200, and F165 (Fig S4c). A total of 1,196 variants were expressed in *E. coli* and screened using whole-cell biotransformation in 96-deep-well plates, followed by product quantification via HPLC. Although substitutions such as L38T, L38I, C167S, and C167T led to further improvements in catalytic activity, no variant outperformed *Ate*HMT-C167A. Iterative saturation mutagenesis (ISM)[31,33] was subsequently applied to construct a double-mutant library (C167A/L38NNK); however, no double mutant with enhanced activity was identified. Therefore, *Ate*HMT-C167A was selected as the final engineered variant for methylation of **1A** (Fig. 2b).

For substrate **1a**, a similar strategy was applied. Briefly, substrate **1a** was directly docked into the active site of *Ate*HMT–SAH, and twenty-two residues within 5 Å of the docked **1a**—A168, W27, M11, P39, W40, L38, C167, V264, T164, P209, P210, R200, F165, Y163, L196, F198, Q273, D274, G265, N46, H262, and T261—were selected for SSM. (Fig S4d) A total of 2,024 variants were expressed in *E. coli* and screened using whole-cell biotransformation in 96-deep-well plates, followed by product quantification via HPLC. Positive mutants were identified in five libraries (M11, V264, L38, H262 and G265). Among these, M11V exhibited the highest catalytic activity relative to the wild-type enzyme, with a conversion rate of 1.96%. Consequently, M11V was selected as the template for ISM with the remaining four positively identified sites.

Four double-mutant libraries (M11V/V264NNK, M11V/L38NNK, M11V/H262NNK and M11V/G265NNK) were constructed and screened. From this round, a double mutant, M11V/V264G (VG),

was identified, achieving a conversion rate of 10.21% toward substrate **1a** (22-fold improvement). However, further iterative mutation of the remaining three sites using VG as the template did not yield variants with improved activity.

As the catalytic efficiency of VG was still unsatisfactory, the screening scope was expanded to 7 Å radius in the second evolutionary round. Residues K4, V6, A7, P8, L15, C37, D41, R42, L169, E197, G208, W211, E263, K266 and R275 were subjected to SSM based on VG. (Fig S4e) Using NNK-based mutagenesis, a total of 1,380 variants were screened, leading to identification of a triple mutant, K4V/M11V/V264G (VVG), which increased the conversion rate of substrate **1a** to 19.71% (43-fold improvement). Further iterative mutation of the remaining sites did not result in additional positive effects. At this stage, additional beneficial mutations were found to be located at the *N*-terminus, suggesting that the *N*-terminal loop1 may play a pivotal role in recognition of the bulky substrate.

Structural analysis revealed loop1 (PPKAVAP) as a highly flexible region nearby the active site (Fig S3a). We hypothesized that stabilizing this loop could further enhance activity toward **1a**. Because proline residues often contribute to protein rigidity and stability, iterative mutagenesis excluded proline at positions 2, 3, and 8. In addition, mutations at V6 and A7 were found to be ineffective; therefore, only residue A5 was selected for further mutagenesis based on the VVG template (Fig S4f). Following NNK-based ISM at A5, a quadruple mutant, K4V/A5L/M11V/V264G (VLVG), was obtained, achieving a conversion rate of 32.04% toward substrate **1a** (71-fold improvement). Accordingly, the VLVG variant was designated *Ate*HMT-VLVG and chosen as the final optimized catalyst for substrate **1a** (Fig. 2c).

To further enhance reaction performance, reaction parameters—including pH, temperature, cosolvent ratio, and substrate ratio—were optimized (Fig. S5). For **1A**, under conditions of pH 8.0, 30 °C, 6% DMSO, and a molar ratio of **1A** : SAH : MeI of 1:1:15, the conversion rate increased to 45.67% (18-fold higher than the *Ate*HMT-WT enzyme). For substrate **1a**, under conditions of pH 8.0, 30 °C, 15% DMSO, and a molar ratio of **1a** : SAH : MeI of 1:1:15, the conversion rate reached 73.36% (162-fold higher than the

164 *Ate*HMT-WT enzyme) (Fig. 2d and Fig. S6). This efficiency is comparable to that reported in systems
165 employing direct SAM addition as the methyl donor[41]. Notably, the system exhibited considerable catalytic
166 activity even with the addition of trace amounts of SAH or in its absence, achieving a conversion rate of
167 over 30% for substrate 1a. (Fig. S5g-h) This result indicates that only trace amounts of the cofactor SAH are
168 required to efficiently drive the regeneration cycle of the methyl donor in vivo, thereby significantly
169 reducing reaction costs and further confirming the great potential of this mutant in methylation applications.

170 ## Identification of the rate-determining step

171 As the overall catalytic process comprises two sequential reactions—MeI + SAH → SAM + I^- and
172 SAM + **1A** or **1a** → SAH + Methylated product—it is necessary to compare these two steps in the
173 *Ate*HMT-WT and mutant enzymes toward the corresponding substrates to identify the rate-limiting step.
174 Accordingly, steady-state kinetic characterization was performed for *Ate*HMT-WT, *Ate*HMT-C167A, and
175 *Ate*HMT-VLVG toward substrates **1A** and **1a**, respectively. As summarized in Table S8, for the SAM
176 regeneration step, both the *Ate*HMT-C167A and *Ate*HMT-VLVG mutants exhibited higher catalytic
177 efficiencies than the *Ate*HMT-WT (k_{cat} values of 323.80 ± 26.76, 157.18 ± 15.84 and 83.30 ± 8.80 min^{-1} for
178 *Ate*HMT-C167A, *Ate*HMT-VLVG and *Ate*HMT-WT, respectively), albeit with reduced affinity for SAH (K_m
179 values of 8.23 ± 1.31, 3.64 ± 0.78 and 2.71 ± 0.91 mM, respectively), indicating that higher SAH
180 concentrations are required to achieve the optimal reaction performance. In contrast, for the second
181 methyl-transfer step, the activity of the *Ate*HMT-WT toward both substrates was too weak to allow reliable
182 determination of kinetic parameters. Notably, the *Ate*HMT-C167A mutant (k_{cat} = 0.09 ± 0.00 min^{-1}, K_m =
183 0.24 ± 0.03 mM, k_{cat}/K_m = 0.38 s^{-1} M^{-1}) and the *Ate*HMT-VLVG mutant (k_{cat} = 0.05 ± 0.00 min^{-1}, K_m = 0.05
184 ± 0.01 mM, k_{cat}/K_m = 1.00 s^{-1} M^{-1}) displayed moderate catalytic activity toward substrates **1A** and **1a**,
185 respectively (Fig. S9 and Tab. S8).

186 Comparison of the two steps clearly indicates that the second reaction proceeds with a substantially
187 lower velocity, identifying it as the rate-determining step. However, the lower K_m values for the final

acceptors relative to SAH in both mutants suggest that pocket reshaping facilitates binding of the second methyl acceptor. Consistent with these observations, turnover number (TON) measurements under optimal conditions showed that both mutants substantially outperformed the *Ate*HMT-WT. For the conversion of **1A** to **2A**, the *Ate*HMT-C167A mutant achieved a TON of 19, representing a 19-fold increase over the *Ate*HMT-WT (TON = 1). Similarly, for the conversion of **1a** to **2a**, the *Ate*HMT-VLVG mutant reached a TON of 25, whereas the *Ate*HMT-WT exhibited a TON of less than 1 due to its extremely low activity (Tab. S9).

Molecular mechanism investigation

To elucidate the molecular basis underlying the enhanced activities of *Ate*HMT-C167A and *Ate*HMT-VLVG toward **1A** and **1a**, respectively, we determined the crystal structures of the *Ate*HMT-C167A–SAH–**1A** and *Ate*HMT-VLVG–SAH–**1a** complexes at resolutions of 2.00 Å and 1.85 Å, respectively (Fig. 3a–3c and Tab. S11). This represents the first report of a ternary complex crystal structure for a halide methyltransferase, and the high-quality electron density permitted unambiguous assignment of both **1A** and **1a** within the active sites.

In the structure of the *Ate*HMT-C167A–SAH–**1A** complex, **1A** is bound within a relatively shallow groove (Fig. 3a). Owing to the high flexibility of residues 1–6, loop1 does not contribute to the formation of the active site or substrate binding. The aromatic plane of **1A** engages in hydrophobic interactions with M11, T164, P210, F198, V264 and loop2 (Fig. 3b). The 7-OH of **1A** forms hydrogen bonds with the side chains of Y163 and R42, which likely accounts for the exclusive formation of a single monomethylated product despite the symmetrical nature of **1A**. Notably, the *Ate*HMT-C167A mutation does not appear to directly participate in **1A** binding, as it is located more than 5 Å from the substrate and does not induce observable conformational changes within the binding pocket. Consistent with this observation, **1A** adopts the same binding mode in the crystal structure of the *Ate*HMT-WT–SAH–**1A** complex (Fig. S10a). These results suggest that the enhanced catalytic activity of *Ate*HMT-C167A toward **1A** arises primarily from more

efficient SAM regeneration, in agreement with the higher k_{cat} value of the *Ate*HMT-C167A mutant in the SAM regeneration step. To further investigate differences in SAM regeneration efficiency, we determined the structures of the *Ate*HMT-C167A–SAH–MeI and *Ate*HMT-WT–SAH–MeI complexes at resolutions of 2.5 Å and 2.0 Å, respectively (Fig 3c, 3d, S10b and Tab. S11). In both structures, MeI adopts a similar "iodide-out" orientation, with its binding site overlapping that of **1A** (Fig. 3c). In *Ate*HMT-WT, however, the thiol group of C167 forms a van der Waals interaction (S–C dipole-induced dipole interaction) with the methyl group of MeI, positioning it 3.7 Å from the C167 sulfur and 4.5 Å from the SAH sulfur (Fig. 3d and Fig. S10b). Loss of this interaction in the *Ate*HMT-C167A mutant results in a shift of the methyl group away from the *Ate*HMT-C167A site and closer to the SAH sulfur, reducing the distance to 4.1 Å. Collectively, these structural observations indicate that the increased catalytic efficiency of *Ate*HMT-C167A is attributable to an accelerated SAM regeneration rate resulting from a shortened methyl–sulfur distance.

Structural comparison of the *Ate*HMT-VLVG–SAH–**1a** with *Ate*HMT-WT–SAH reveals no major global rearrangements, except for the *N*-terminal loop (loop1), which adopts a distinct conformation upon **1a** binding (Fig. 3e). This conformational change induces a 1.8 Å displacement of the adjacent α-helix harboring the M11V mutation. Substrate **1a** is accommodated within a narrow and deep cavity, with loop1 extending along the elongated molecular framework of **1a** from the chromenone moiety to the phenol moiety, thereby directly contributing to substrate recognition through water-mediated hydrogen bonding (V6) and hydrophobic interactions (A5L) (Fig. 3f). Although the K4V mutation does not directly participate in pocket formation or substrate binding, the reduced polarity and conformational entropy introduced by this substitution may facilitate stabilization of loop1. The M11V and V264G mutations are positioned at opposite ends of the binding pocket, and their reduced side-chain volumes create additional space to accommodate the chromenone and phenol rings of **1a**, respectively, explaining their critical roles in the initial enhancement of *Ate*HMT activity toward **1a**. The phenol ring of **1a** is further stabilized through a cation–π interaction with the side chain of R42 (loop2) on one side and hydrophobic interactions with A5L

and F198 on the other. The chromenone ring is further anchored by a second water-mediated hydrogen bond between the 7-OH group and the backbone carbonyl of T164. Together, these interactions position 7-*O* of **1a** as the atom closest to the SAH sulfur, at a distance of 4.8 Å. In summary, the high methylation activity of *Ate*HMT-VLVG toward **1a** arises from a synergistic combination of binding-pocket reconfiguration driven by loop1 conformational changes and pocket enlargement achieved through substitutions with smaller side-chain residues.

Exploration of *Ate*HMT Family Members and Mechanism-Guided Rational Design

To investigate whether *Ate*HMT is unique in possessing substrate-coupling catalytic properties, we performed a BLAST search to identify homologous proteins. The top 1,000 sequences with the highest sequence identity, together with eight previously reported HMTs[18,21,27,42], were selected to construct a sequence similarity network (SSN). Notably, seven previously reported HMTs (highlighted in bright yellow) did not cluster with *Ate*HMT. In contrast, the initial template enzyme *Acl*HMT—used to mine *Ate*HMT—was unexpectedly located within the same family, despite having never been reported to exhibit substrate-coupling activity. To verify the reliability of the SSN analysis and considering the structural diversity of natural methyl acceptors, we selected **1a** as the probe substrate, reasoning that HMTs with high sequence homology would be more appropriate candidates. Accordingly, ten HMTs from this family (labeled in cyan: *Aam*HMT (89.36% identity), *Aho*HMT (77.94% identity), *Aja*HMT (76.16% identity), *Avi*HMT (75.80% identity), *Afi*HMT (79.20% identity), *Ati*HMT (78.49% identity), *Abr*HMT (79.93% identity), *Ale*HMT (78.85% identity), *Auv*HMT (76.87% identity), and *Ain*HMT (76.51% identity) together with *Acl*HMT (72.34% identity, highlighted in bright yellow), were chosen for activity assays (Fig. 4a, S11 and Tab. S10). Enzymatic reactions were conducted under standard conditions, and gratifyingly, all tested HMTs exhibited detectable activity toward **1a**, although conversions were generally below 2% (Fig. 4b).

To assess whether the activity-regulation mechanism identified in *Ate*HMT is transferable across the family, we performed mechanism-guided engineering on five additional HMTs. Based on our mechanistic

insights, we hypothesized that the same loop1 would modulate reactivity toward **1a** in related enzymes. Accordingly, representative HMTs were selected, and the corresponding mutations were introduced at homologous positions. The catalytic activities of these variants were then evaluated to determine the generality of the regulatory mechanism. As shown in Fig. 4c, enzymes sharing >78.5% sequence identity with *Ate*HMT (*Ale*HMT and *Aam*HMT) exhibited significant activity enhancement upon introduction of the *Ate*HMT-VLVG mutation, with the degree of improvement positively correlated with sequence homology. In contrast, for enzymes with <78.5% homology (including *Acl*HMT, *Aho*HMT and *Ati*HMT), the same mutations resulted in no obvious improvement or even slight decreases in activity (Fig. S13). These results suggest that, although these enzymes share common catalytic functions and high overall homology, engineering strategies based solely on sequence conservation are limited, and structure-guided approaches are likely to be more reliable. Notably, several wild-type enzymes (*Abr*HMT, *Ati*HMT and *Acl*HMT) displayed higher intrinsic activity toward **1a** than *Ate*HMT-WT, highlighting their potential as superior starting points for future directed evolution.

Overall, the identification of an HMT family with substrate-coupling properties provides a valuable resource for further exploration. Although only substrate **1a** was evaluated here, other family members may possess distinct activities toward diverse molecular scaffolds. By integrating directed evolution with AI-assisted enzyme design, we anticipate that highly efficient HMTs with robust substrate-coupling catalytic activity can be developed from this enzyme family.

Substrate-Scope Exploration

To assess the synthetic utility of the *Ate*HMT-based iodomethane-coupled methylation system, we investigated its substrate scope and performance at preparative scale. To improve operational simplicity and economic feasibility, an *E. coli* chassis strain lacking the *mtn* gene encoding SAH hydrolase was constructed[43,44], thereby preventing degradation of the SAH substrate. Using this chassis, catalytic assays were first conducted on the model substrate **1a** with cell lysates prepared from whole cells at a defined

OD_{600} of 120. Notably, lysates from the *mtn*-knockout strain substantially increased product formation relative to the parental strain and maintained a high conversion (83%) even at an elevated substrate concentration of 2 mM. For substrate **1A**, under the same condition of 2 mM substrate concentration, the lysate of the gene-knockout strain also exhibited a certain improvement (48%) when the OD_{600} of 80, highlighting the robustness of the single-enzyme, iodomethane-coupled methylation system under synthetically relevant conditions. (Fig. S15) On the basis of these favorable properties, cell lysates prepared from the engineered *E. coli* chassis under these conditions were subsequently employed for all substrate-scope investigations and preparative-scale reactions.

For the mutant *Ate*HMT-C167A, seven naphthol derivatives bearing hydroxyl groups at distinct positions were selected based on the structural features of substrate **1A**. These substrates include compounds with hydroxyl groups located on different benzene rings (**1B**–**1D**) and on the same benzene ring (**1E**–**1H**). Activity assays showed that both *Ate*HMT-WT and *Ate*HMT-C167A exhibited detectable activity toward **1B**–**1D** and **1H**, whereas no reaction was observed for **1E**–**1G**, indicating a pronounced positional preference for hydroxyl substitution on the naphthalene scaffold. For substrates **1B**–**1D**, the *Ate*HMT-C167A mutant displayed varying degrees of activity enhancement relative to the *Ate*HMT-WT, while for substrate **1H** its activity was reduced compared with *Ate*HMT-WT. Notably, **1H** is the only substrate bearing two hydroxyl groups on the same aromatic ring that is accepted by the enzyme. By contrast, **1G** also contains two adjacent hydroxyl groups but exhibits no detectable activity. This difference in catalytic behavior is consistent with the observations in the *Ate*HMT-C167A-SAH-**1A** structure, in which the 5-C and 6-C positions of **1A** are exposed to the solvent and there is sufficient space in front of 3-C to accommodate small chemical groups such as Br in **1B** and hydroxyl group in **1H**. For **1H**, addition a 3-OH may also form a hydrogen bond with the main chain of P209 to stabilize **1H**. Meanwhile, the C1 and C8 positions are oriented toward the side chain of T164, with the closest interatomic distance of approximately 4.2 Å, suggesting that substitution at these positions may induce steric clashes between the protein and the

substrate. Consistent with this interpretation, substrate **1G** contains a 1-hydroxyl group, which may push the adjacent 2-hydroxyl group away from the SAH sulfur, thereby disrupting productive methyl transfer and resulting in inactivity (Fig S16).

For the mutant *Ate*HMT-VLVG, we selected 29 structurally diverse medicinal flavonoids, categorized into six classes—flavanonols (I), flavones (II), flavonones (III), stilbenes (IV), isoflavones (V), and dihydroflavonols (VI)—together with one anthraquinone substrate (VII) (Fig. 5), to perform a systematic activity assessment. The results indicated that *Ate*HMT-VLVG exhibited superior catalytic activity relative to the *Ate*HMT-WT across all tested substrates and largely retained comparable regioselectivity; notably, 17 out of 26 tested substrates displayed identical product distributions.

For Type I substrates (**1b**–**1g**), both *Ate*HMT-WT and *Ate*HMT-VLVG showed detectable activity toward all tested compounds. *Ate*HMT-WT exhibited low activity toward **1e** and **1f** and moderate activity toward **1b**–**1d** and **1g**. In contrast, *Ate*HMT-VLVG displayed markedly enhanced activity, particularly for **1b**–**1d** and **1g**, with total conversion rates exceeding 60%. For the poorer substrates **1e** and **1f**, *Ate*HMT-VLVG afforded approximately 20-fold and 5-fold activity enhancements, respectively. Product composition analysis using authentic standards revealed that both variants preferentially catalyzed methylation at the 7-*O* position, with the 5′-hydroxyl group serving as a secondary methylation site. Consequently, 7-*O*- and 5′-*O*-monomethylated products accounted for more than 85% of the total products for substrates such as **1b**, **1d**, and **1g**. When the 5′-hydroxyl group was pre-methylated (**1c**) or absent (**1e**, **1f**), nearly exclusive formation of the 7-*O*-methylated product was observed. In addition, **1d**, which lacks a 5-hydroxyl group, yielded 3-*O*-methylated products. Overall, the *Ate*HMT-VLVG mutations did not substantially alter regioselectivity but significantly increased catalytic activity, thereby enabling the formation of multisite-methylated products.

For Type II and III substrates (**1h**–**1r**), both *Ate*HMT-WT and *Ate*HMT-VLVG exhibited reduced conversion rates relative to Type I substrates, although *Ate*HMT-VLVG consistently showed superior

catalytic performance. Notably, for substrates **1h**, **1m**, and **1o**, *Ate*HMT-VLVG achieved conversions of up to 20%, representing a clear improvement over *Ate*HMT-WT, which showed weak or undetectable activity. Two substrates (**1k** and **1l**) were unstable under the reaction conditions and could not be detected after the reaction, precluding quantitative conversion analysis. The markedly reduced activity toward Type II and III substrates is likely attributable to the absence of the 3-hydroxyl group, underscoring the importance of the water-mediated hydrogen bond between the 3-OH group and V6 in substrate recognition. Despite reduced activity, regioselectivity was largely conserved. In addition to predominant 7-*O*-methylation on the A-ring, methylation at the 6-*O* position was detected for certain substrates (**1k**, **1l, 1o**). Dimethylated products (**4i**, **4k**, and **4l**) were also identified among Type II and III substrates. For other substrates with potential dimethylation sites, corresponding products were not detected, presumably due to insufficient catalytic activity. Notably, for substrates **1i** and **1j**, *Ate*HMT-VLVG altered regioselectivity from 5′-*O* methylation (*Ate*HMT-WT) to preferential 7-*O* methylation. To elucidate this behavior, substrates **1i** was docked into the active sites of *Ate*HMT-WT-SAH (Fig S17a). The result shows that the catechol group of **1i** is bound in a similar way to that of **1A**, with their corresponding atoms overlapping well. Additionally, the ortho-hydroxyl group of **1i** forms a hydrogen bond with the main chain of P209. In **1i** and **1j**, this hydroxyl group is modified with a methyl group, which leads to disruption of the hydrogen bond and lower catalytic activity.

For Type IV substrates, *Ate*HMT-WT showed no detectable activity, whereas *Ate*HMT-VLVG exhibited weak but measurable reactivity. Product analysis against commercial standards confirmed exclusive formation of the 5-*O*-methylated product. The limited activity is likely attributable to the linear molecular architecture of these substrates, as the enzyme displays a preference for substrates with more parallel ring arrangements.

For Type V substrates (**1t**–**1x**), all five compounds were accepted as substrates, although their catalytic efficiencies varied substantially. Only **1t** and **1u** exhibited relatively high conversion rates, while the remaining substrates showed conversions below 5%. Product analysis revealed predominant methylation at

the 7-*O* position. Trace amounts of dimethylated products were detected for substrate **1w**, whereas no dimethylation was observed for **1t**, which contains a 5-OH group. We therefore propose that the presence of a 5-OH group influences substrate binding orientation within the active pocket, thereby modulating methylation patterns.

Type VI dihydroflavonols exhibited catalytic activity and regioselectivity comparable to those observed for substrate **1q**. *Ate*HMT-WT afforded approximately 20% conversion, while *Ate*HMT-VLVG achieved approximately 30% conversion. Similar to substrates **1i** and **1j**, *Ate*HMT-WT favored 5′-*O*-methylation, whereas *Ate*HMT-VLVG shifted selectivity toward 7-*O*-methylation, likely due to a similar binding mode.

For the Type VII anthraquinone substrate, *Ate*HMT-VLVG increased the conversion rate to approximately 30%, compared with ~5% for *Ate*HMT-WT. Both variants displayed exclusive 2-*O*-methylation selectivity. Docking analyses indicated that the enhanced activity and strict regioselectivity arise from favorable positioning of the reactive hydroxyl group within the remodeled active pocket, similar to that of **1a** in the *Ate*HMT-VLVG-SAH-**1a** structure (Fig. S17b).

Based on analysis of flavonoid substrates from Types I, II, III, and V, we inferred that the presence of a hydroxyl group on the A-ring is critical for substrate recognition by *Ate*HMT variants. To validate this hypothesis, substrates **1aa**–**1ad** bearing a single hydroxyl group on either the A-, B-, or C-ring were examined (substrates with 8-hydroxyl substitution were excluded due to unavailability). None of these substrates exhibited detectable activity, supporting our hypothesis. Unlike **1aa** and **1ac**–**1ad**, substrate **1ab** contains a 5-OH group; however, the adjacent ketone group likely forms an intramolecular hydrogen bond that reduces the nucleophilicity of the 5-OH group. Together with the results obtained for substrates **1n** and **1o**, these findings indicate that hydroxyl groups on the A-ring—excluding the 5-position—are essential for substrate recognition.

Overall, *Ate*HMT exhibits a remarkably broad substrate scope, and engineering for enhanced activity

while maintaining promiscuous selectivity establishes it as a promising template for further evolution, paving the way toward biomanufacturing of rare methylated products.

To further assess the practical applicability of this methylation platform, compounds **1a** and **1c** were synthesized using the engineered *E. coli* (Δ*mtn*) strain as a whole-cell catalyst. This strategy was successfully implemented, and as shown in Fig. 6, all target products were obtained at the milligram scale, demonstrating the preparative utility of this single-enzyme methylation system (Fig. S18). Notably, product **2a** is the natural product rhamnocitrin, which exhibits diverse pharmacological activities, including inhibition of IGF-1R signaling, induction of apoptosis in human nasopharyngeal carcinoma cells[45], regulation of the Wisp2-mediated PPARγ/NF-κB/TGF-β1/Smad2/3 signaling pathway, and attenuation of ovarian granulosa cell fibrosis[46]. Product **2c**, rhamnetin, is another bioactive natural product with demonstrated therapeutic potential against cancers, viral infections, inflammatory diseases, and other conditions through inhibition of protein kinase CK22[47]. Importantly, this synthetic platform operates efficiently without exogenous SAM supplementation or complex multi-enzyme cascades. Further optimization of this cell factory is expected to enable large-scale production of rare, functionally methylated compounds.

CONCLUSION

Here we identify a previously unrecognized family of halide methyltransferases (HMTs) and establish a paradigm shift from the classical HMT–MT cooperative methylation to a single-HMT–enabled, cost-effective methylation platform. Through rational enzyme mining, directed evolution, and expansion of family members, we provide a rich resource for fundamental and applied studies of methyltransferases. Kinetic dissection of the two catalytic steps, together with 6 crystal structures (*Ate*HMT-WT–SAH, *Ate*HMT-WT–SAH–MeI, *Ate*HMT-WT–SAH–**1A**, *Ate*HMT-C167A–SAH–**1A**, *Ate*HMT-C167A–SAH–MeI and *Ate*HMT-VLVG–SAH–**1a**), elucidates the molecular basis of substrate specificity, catalytic activity, and regioselectivity. These analyses reveal how cofactor regeneration and

active-site dynamics cooperatively govern methylation efficiency. Distinct substrate-specificity mechanisms were observed for the two model substrates, **1A** and **1a**. For **1A**, a planar molecule that can directly access the active site, the enhanced activity of the C167A variant primarily arises from improved efficiency of SAM regeneration. In contrast, **1a**, which adopts a more sterically demanding conformation, requires a substrate-induced reorganization of a unique *N*-terminal loop (loop1) to facilitate binding. This loop captures the substrate and positions it closer to the reactive center. In the *Ate*HMT-VLVG variant, mutations stabilize this loop in a refolded conformation, enabling more effective substrate positioning and directing it toward the catalytic site for methyl transfer. Notably, the engineered HMT displays broad substrate scope and robust catalytic performance, enabling preparative-scale access to rare methylated products, as validated by systematic substrate-scope studies and scale-up reactions.

Beyond this work, single-enzyme HMT catalysis offers a decisive advantage over dual-enzyme methylation systems, which typically require laborious optimization of enzyme compatibility and reaction conditions. The discovery of this HMT family thus provides a streamlined and versatile platform for methylation biocatalysis. Importantly, it opens a fast track for the development and engineering of alternative, artificial methyl carriers to replace expensive and unstable SAM, substantially expanding the practical and industrial potential of HMT-based transformations.

REFERENCES

1 Farajat, D., Zhang, Y. & Li, C.-J. Magic methylation with methyl-containing peroxides. *Chem. Sci.* **16**, 507-529 (2025).

2 Schönherr, H. & Cernak, T. Profound methyl effects in drug discovery and a call for new C-H methylation reactions. *Angew. Chem. Int. Ed.* **52**, 12256-12267 (2013).

3 Fiorani, G., Perosa, A. & Selva, M. Dimethyl carbonate: A versatile reagent for a sustainable valorization of renewables. *Green Chem.* **20**, 288-322 (2018).

4 Chen, Y. Recent advances in methylation: A guide for selecting methylation reagents. *Chem. Eur. J.* **25**, 3405-3439 (2019).

5 McKean, I. J. W., Hoskisson, P. A. & Burley, G. A. Biocatalytic alkylation cascades: Recent advances and future opportunities for late-stage functionalization. *ChemBioChem* **21**, 2890-2897 (2020).

6 Wu, S., Snajdrova, R., Moore, J. C., Baldenius, K. & Bornscheuer, U. T. Biocatalysis: Enzymatic synthesis for industrial applications. *Angew. Chem. Int. Ed.* **60**, 88-119 (2021).

7 Hauer, B. Embracing nature's catalysts: A viewpoint on the future of biocatalysis. *ACS Catal.* **10**, 8418-8427 (2020).

8 Bennett, M. R., Shepherd, S. A., Cronin, V. A. & Micklefield, J. Recent advances in methyltransferase biocatalysis. *Curr. Opin. Chem. Biol.* **37**, 97-106 (2017).

9 Struck, A. W., Thompson, M. L., Wong, L. S. & Micklefield, J. *S*-adenosyl-methionine-dependent methyltransferases: Highly versatile enzymes in biocatalysis, biosynthesis and other biotechnological applications. *ChemBioChem* **13**, 2642-2655 (2012).

10 Wessjohann, L., Dippe, M., Tengg, M. & Gruber-Khadjawi, M. Methyltransferases in biocatalysis. *Cascade Biocatal.* **18**, 393-426 (2014).

11 Jin, J. Q. *et al.* Characterization of two *O*-methyltransferases involved in the biosynthesis of *O*-methylated catechins in tea plant. *Nat. Commun.* **14**, 5075 (2023).

12 Zhang, M. *et al.* Molecular and structural characterization of a chalcone di-*C*-methyltransferase rdcmt from *rhododendron dauricum* and its application in *de novo* biosynthesis of farrerol in *pichia pastoris*. *J. Am. Chem. Soc.* **147**, 17132-17143 (2025).

13 Chen, R. *et al.* Biochemical and structural insights of the *N*-methyltransferase cyaf in cyanogramide biosynthesis. *J. Nat. Prod.* **88**, 715-722 (2025).

14 Abdelraheem, E. *et al.* Methyltransferases: Functions and applications. *ChemBioChem* **23**, e202200212 (2022).

15 Zhang, C., Sultan, S. A., T, R. & Chen, X. Biotechnological applications of *S*-adenosyl-methionine-dependent methyltransferases for natural products biosynthesis and diversification. *Bioresour. Bioprocess.* **8**, 72 (2021).

16 Liao, C. & Seebeck, F. P. *S*-adenosylhomocysteine as a methyl transfer catalyst in biocatalytic methylation reactions. *Nat. Catal.* **2**, 696-701 (2019).

17 Tang, Q. *et al.* Directed evolution of a halide methyltransferase enables biocatalytic synthesis of diverse SAM analogs. *Angew. Chem. Int. Ed.* **60**, 1524-1527 (2021).

18 Gao, C. Y. *et al.* Engineering of halide methyltransferase *Bx*hmt through dynamic cross-correlation network analysis. *Angew. Chem. Int. Ed.* **63**, e202401235 (2024).

19 Rudenko, A. Y. *et al.* Organophosphorus *S*-adenosyl-*L*-methionine mimetics: Synthesis, stability, and substrate properties. *Front. Chem.* **12**, 1448747 (2024).

20 Ju, S. *et al.* A biocatalytic platform for asymmetric alkylation of α-keto acids by mining and engineering of methyltransferases. *Nat. Commun.* **14**, 5704 (2023).

21 Bengel, L. L. *et al.* Engineered enzymes enable selective *N*-alkylation of pyrazoles with simple haloalkanes. *Angew. Chem. Int. Ed.* **60**, 5554-5560 (2021).

22 Hoffmann, A., Schülke, K. H., Hammer, S. C., Rentmeister, A. & Cornelissen, N. V. Comparative *S*-adenosyl-*L*-methionine analogue generation for selective biocatalytic friedel-crafts alkylation. *Chem. Commun.* **59**, 5463-5466 (2023).

23 Xiong, X. *et al.* Structure-guided engineering of a promiscuous *O*-methyltransferase for a SAM regeneration biocatalysis platform of methylated pharmaceuticals. *Adv. Sci.*, e17794 (2025).

24 Gantt, R. W., Peltier-Pain, P., Cournoyer, W. J. & Thorson, J. S. Using simple donors to drive the equilibria of glycosyltransferase-catalyzed reactions. *Nat. Chem. Biol.* **7**, 685-691 (2011).

25 Damian, M., Wei, Z., Tseliou, V. & Mutti, F. G. Single-enzyme redox-neutral oxidation of alcohols to carboxylic acids using alcohol dehydrogenases. *Catal. Sci. Technol.* (2026).

26 Yan, Q. *et al.* From semirational to rational design: Developing a substrate-coupled system of glucose dehydrogenase for asymmetric synthesis. *ACS Catal.* **12**, 6746-6755 (2022).

27 Schülke, K. H., Ospina, F., Hörnschemeyer, K., Gergel, S. & Hammer, S. C. Substrate profiling of anion methyltransferases for promiscuous synthesis of *S*-adenosylmethionine analogs from haloalkanes. *ChemBioChem* **23** (2022).

28 Arnold, F. H. Innovation by evolution: Bringing new chemistry to life (nobel lecture). *Angew. Chem. Int. Ed.* **58**, 14420-14426 (2019).

29 Zeymer, C. & Hilvert, D. Directed evolution of protein catalysts. *Annu. Rev. Biochem.* **87**, 131-157 (2018).

30 Wang, Y. *et al.* Directed evolution: Methodologies and applications. *Chem. Rev.* **121**, 12384-12444 (2021).

31 Qu, G., Li, A., Acevedo-Rocha, C. G., Sun, Z. & Reetz, M. T. The crucial role of methodology development in directed evolution of selective enzymes. *Angew. Chem. Int. Ed.* **59**, 13204-13231 (2020).

32 Turner, N. J. Directed evolution drives the next generation of biocatalysts. *Nat. Chem. Biol.* **5**, 567-573 (2009).
33 Reetz, M. T. Laboratory evolution of stereoselective enzymes: A prolific source of catalysts for asymmetric reactions. *Angew. Chem. Int. Ed.* **50**, 138-174 (2011).
34 Ospina, F. *et al.* Selective biocatalytic *N*-methylation of unsaturated heterocycles. *Angew. Chem. Int. Ed.* **61**, e202213056 (2022).
35 Li, Z., Wen, X., Bolotova, S. B. & Seebeck, F. P. Short-circuiting the SAM-cycle in *Escherichia coli*. *J. Am. Chem. Soc.* **147**, 47690-47700 (2025).
36 Chovancova, E. *et al.* Caver 3.0: A tool for the analysis of transport pathways in dynamic protein structures. *PLOS Comput. Biol.* **8**, e1002708 (2012).
37 Reetz, M. T., Bocola, M., Carballeira, J. D., Zha, D. & Vogel, A. Expanding the range of substrate acceptance of enzymes: Combinatorial active-site saturation test. *Angew. Chem. Int. Ed.* **44**, 4192-4196 (2005).
38 Reetz, M. T., Carballeira, J. D. & Vogel, A. Iterative saturation mutagenesis on the basis of B factors as a strategy for increasing protein thermostability. *Angew. Chem. Int. Ed.* **45**, 7745-7751 (2006).
39 Acevedo-Rocha, C. G., Ferla, M. & Reetz, M. T. Directed evolution of proteins based on mutational scanning. *Methods Mol. Biol.* **1685**, 87-128 (2018).
40 Reetz, M. T. & Carballeira, J. D. Iterative saturation mutagenesis (ISM) for rapid directed evolution of functional enzymes. *Nat. Protoc.* **2**, 891-903 (2007).
41 Shimizu, T. *et al.* Purification and identification of naringenin 7-*O*-methyltransferase, a key enzyme in biosynthesis of flavonoid phytoalexin sakuranetin in rice. *J. Biol. Chem.* **287**, 19315-19325 (2012).
42 Schmidberger, J. W., James, A. B., Edwards, R., Naismith, J. H. & O'Hagan, D. Halomethane biosynthesis: Structure of a SAM-dependent halide methyltransferase from *Arabidopsis thaliana*. *Angew. Chem. Int. Ed.* **49**, 3646-3648 (2010).
43 Zhang, Y. *et al.* Construction and application of an efficient methylation platform in *Escherichia coli* based on SAM regeneration. *Chem. Eng. J.* **512**, 162642 (2025).
44 Li, Z., Wen, X., Bolotova, S. B. & Seebeck, F. P. Short-circuiting the SAM-cycle in *Escherichia coli*. *J. Am. Chem. Soc.* (2025).
45 Zhou, Y.-Y. *et al.* Rhamnocitrin induces apoptosis of human nasopharyngeal carcinoma by inhibiting IGF-1R signaling pathway in vitro. *J. Asian Nat. Prod. Res.* **28**, 112-127 (2026).
46 Zhou, Y. Y. *et al.* Rhamnocitrin decreases fibrosis of ovarian granulosa cells by regulating the activation of the PPARγ/NF-κB/TGF-β1/Smad2/3 signaling pathway mediated by wisp2. *Ann. Transl. Med.* **10**, 789 (2022).
47 Golub, A. G. *et al.* Discovery and characterization of synthetic 4′-hydroxyflavones—new CK2 inhibitors from flavone family. *Biorg. Med. Chem.* **21**, 6681-6689 (2013).

Acknowledgements

J. W. acknowledge the financial support from the National Key Research and Development Program of China (No. 2023YFA0914100/2023YFA0914102), the National Natural Science Foundation of China (22477110 and 22034002), and the Fundamental Research Funds for the Central Universities (226202400061 and 226202300100). Z.-M. Z. acknowledges the finance support from Guangdong Major Project of Basic and Applied Basic Research (2023B0303000026) and Guangdong basic and applied basic research foundation (2024B1515040007). We thank the staffs from BL19U1 beamline and of National Facility for Protein Science in Shanghai (NFPS) and BL02U1 at Shanghai Synchrotron Radiation Facility,

for assistance during data collection.

Data availability

The data that support the findings of this study are available within the paper and its Supplementary Information, or are available from the corresponding authors upon reasonable request. Source data are provided with this paper.

Author contributions

Z.-M. Z. and J. W. conceived the project, wrote and revised the manuscript. J. C. contributed to drafting and revising the manuscript. J. C. and S. T. carried out the cloning and expression of the PTs, protein purification, biochemical kinetics, chemical synthesis, purification and analysis of the products. J. C., P. L. and S. T. contributed equally. The article was written on the basis of contributions of all authors. All authors approved the final version of the article.

Competing interests

The authors declare no competing interests.

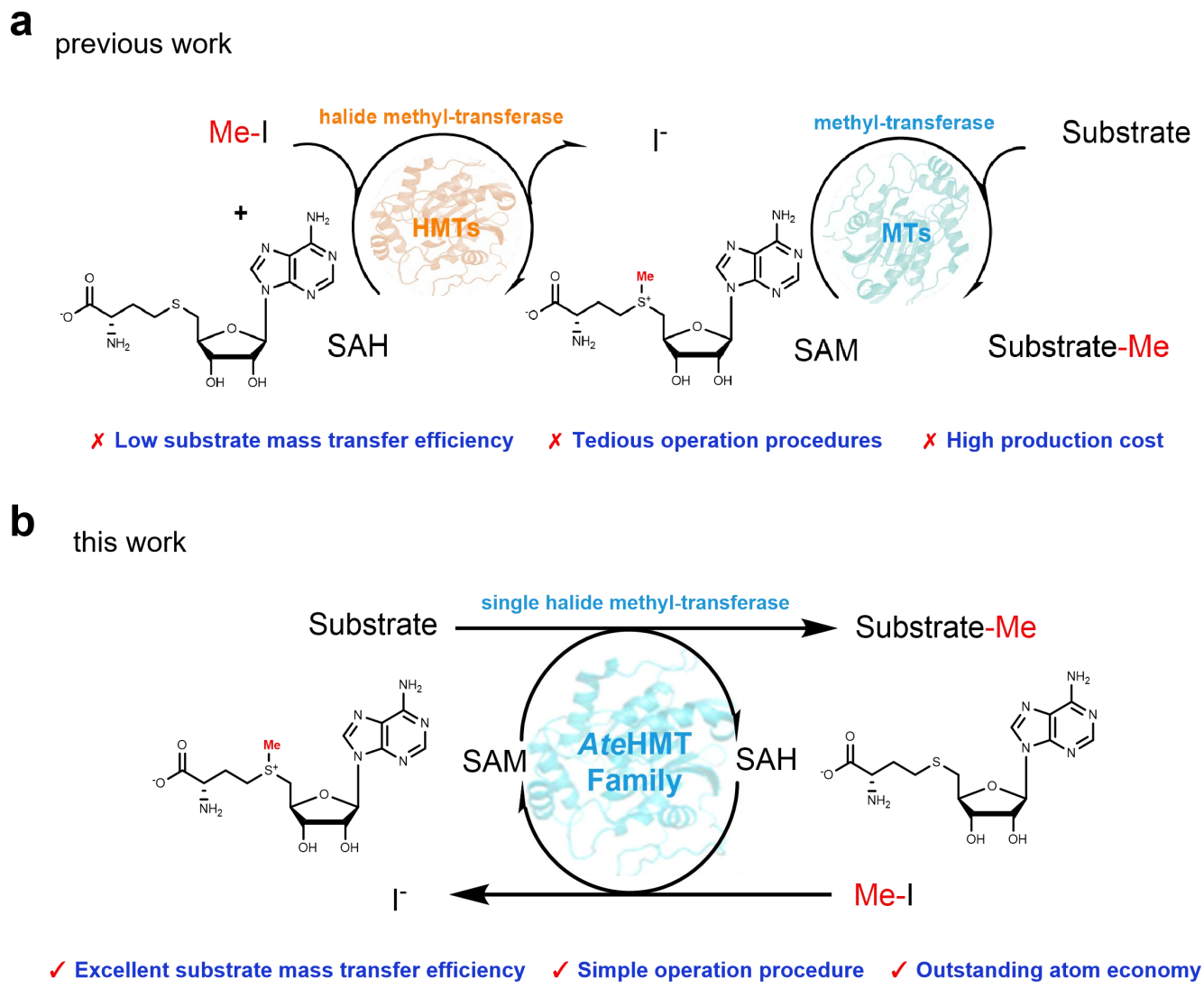

Fig.1 Biocatalytic methylation technology mediated by methyl-transferases. a, Schematic of the conventional two-enzyme cascade methylation strategy, co-catalyzed by halide methyl-transferases (HMTs) and methyl-transferases (MTs). HMTs regenerate the methyl donor SAM, while MTs transfer methyl groups to substrates for methylation modification, which suffers from low mass transfer efficiency, tedious operation and high cost. **b**, The single-enzyme catalytic methylation system based on the *Ate*HMT family discovered in this work integrates SAM regeneration and methyl transfer into a single enzymatic step, achieving efficient substrate mass transfer, simplified operation and outstanding atom economy.

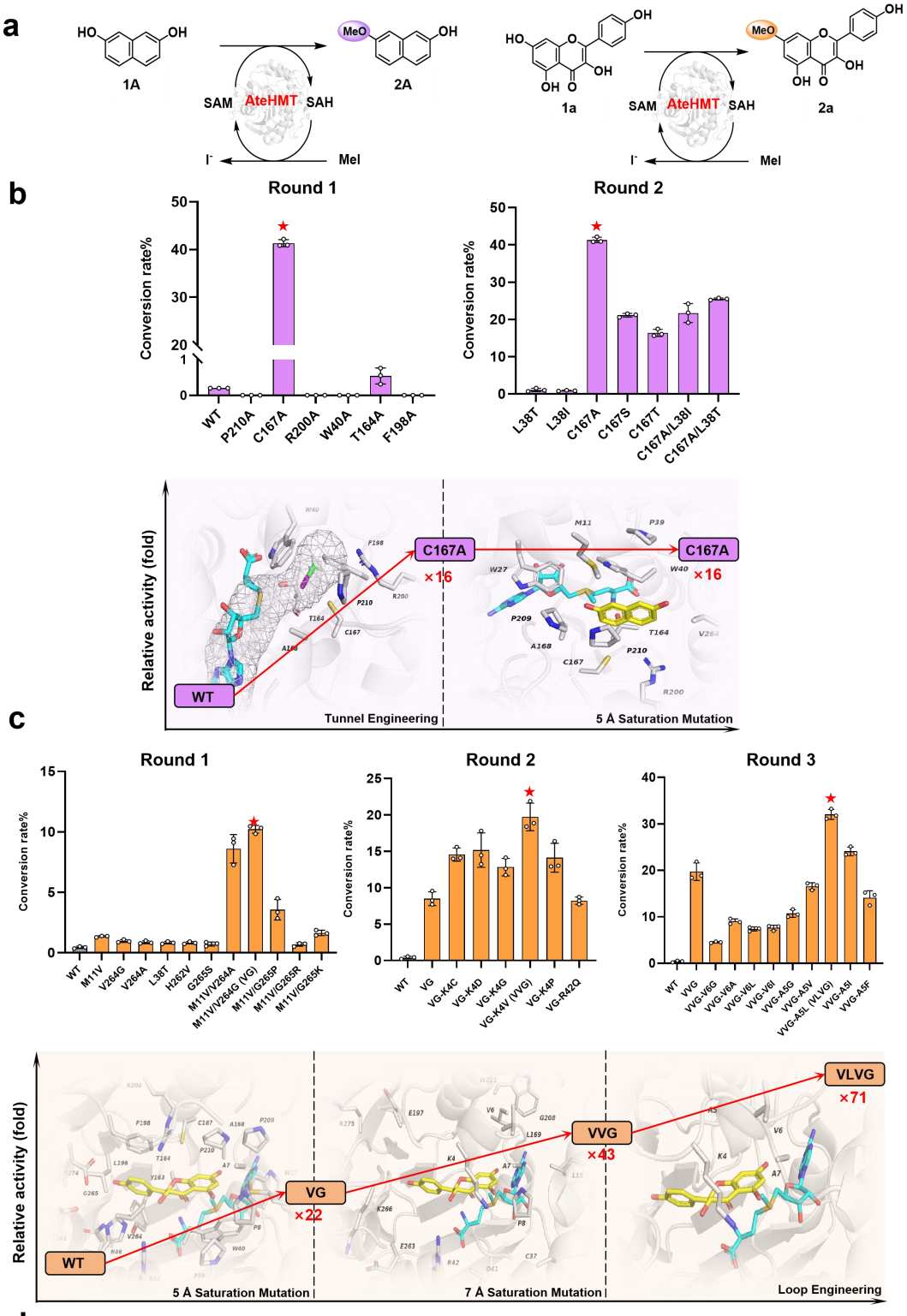

d

entry	variants	2A yield	2a yield	fold activity increase
1	WT	2.54%	0.45%	
2	C167A	41.33%		16
3	C167A pH 8.0, 30 °C, DMSO 6%	45.67%		18
4	VLVG		32.04%	71
5	VLVG pH 8.0, 30 °C, DMSO 12%		73.36%	162

Fig.2 Directed evolution of *Ate*HMT for methylation of 1A and 1a. a, Model reactions: Conversion of 2,7-dihydroxynaphthalene (**1A**) to 7-methoxy-2-naphthol (**2A**) and kaempferol (**1a**) to rhamnocitrin (**2a**). **b,** Two-round evolution of *Ate*HMT-WT for conversion of **1A** to **2A**: alanine scanning of MeI-channel residues (Round 1) followed by SSM of 1A-proximal residues (Round 2). **c,** Three-round evolution for conversion of

1a to **2a**: SSM and ISM of 1a-binding residues (Rounds 1–2), followed by SSM of the N-terminal loop (Round 3). Key variants: VG (M11V/V264G), VVG (K4V/M11V/V264G), and VLVG (K4V/A5L/M11V/V264G). Fold improvements relative to WT are shown in red. **d,** Reaction conditions (pH, temperature, DMSO) optimized independently for each mutant set.

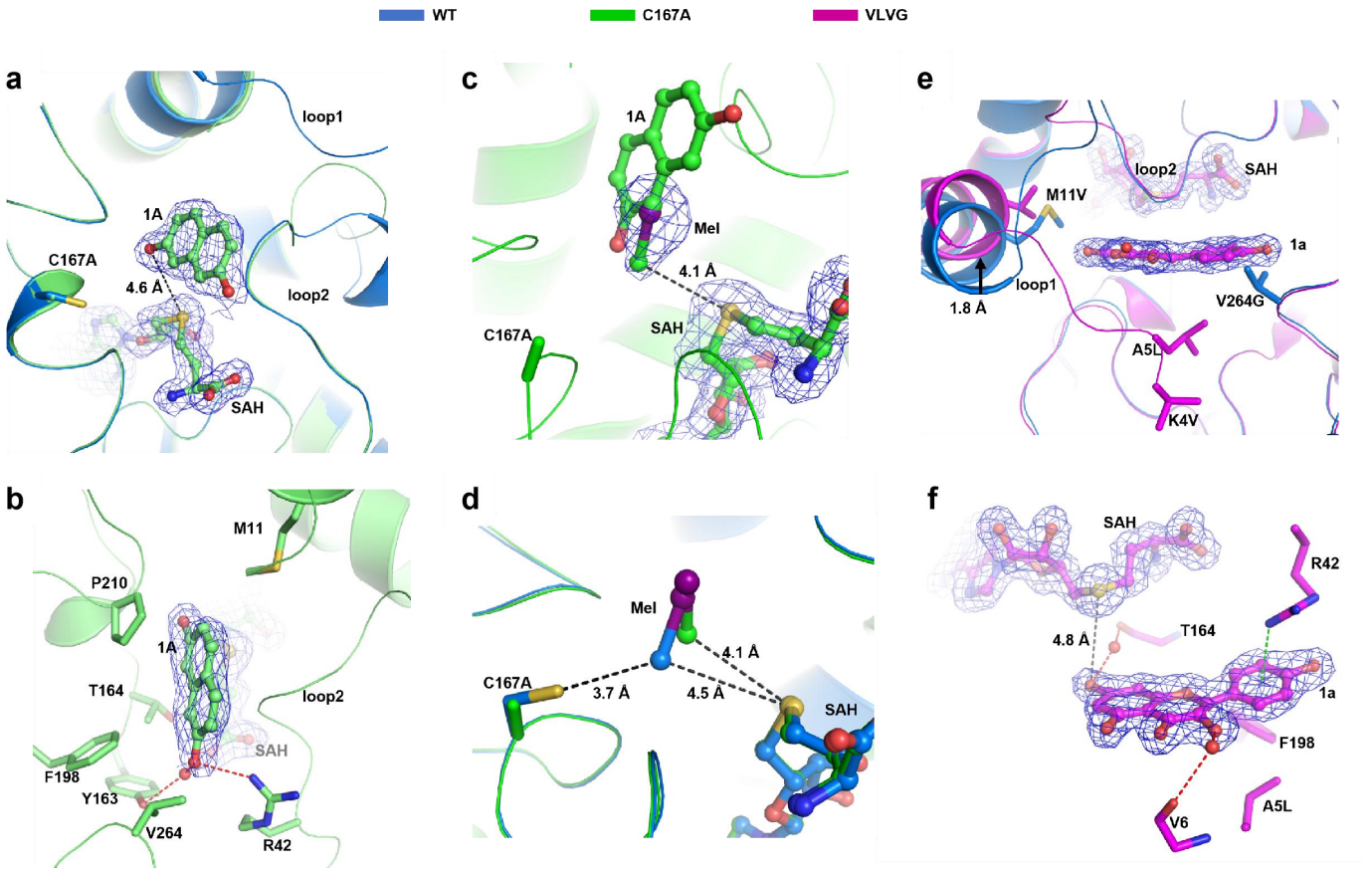

Fig.3 Structural analysis of *Ate*HMT variants. a, Structural overlap of *Ate*HMT-C167A–SAH–**1A** with *Ate*HMT-WT–SAH. 2Fo–Fc omit map of SAH and **1A** contoured at 1.0 σ. **b**, Key residues around the **1A** binding pocket. Hydrogen bonds shown as red dashes. **c**, Comparison of the MeI binding in *Ate*HMT-C167A−SAH−MeI versus **1A** in *Ate*HMT-C167A−SAH−**1A**. The 2Fo-Fc omit map of MeI and SAH is contoured at the σ-level of 1.0. **d**, Comparison MeI binding sites in *Ate*HMT-C167A and *Ate*HMT-WT. **e**, Structural overlap of *Ate*HMT-VLVG−SAH−**1a** with *Ate*HMT-WT−SAH. The mutated residues, SAH and **1a** shown as sticks. Blue mesh: The 2Fo-Fc omit map of SAH and **1a** in the *Ate*HMT-VLVG−SAH−**1a** complex is contoured at the σ-level of 1.0. The α-helix following the N-terminal loop moves approximately 1.8 Å after **1a** binding. **f**, Key interactions between **1a** and surrounding residues. Hydrogen bonds, cation-π interaction and the O-S distance shown as red, orange and black dashes, respectively. The distance between SAH sulfur and the C7 hydroxyl group shown as a black dash.

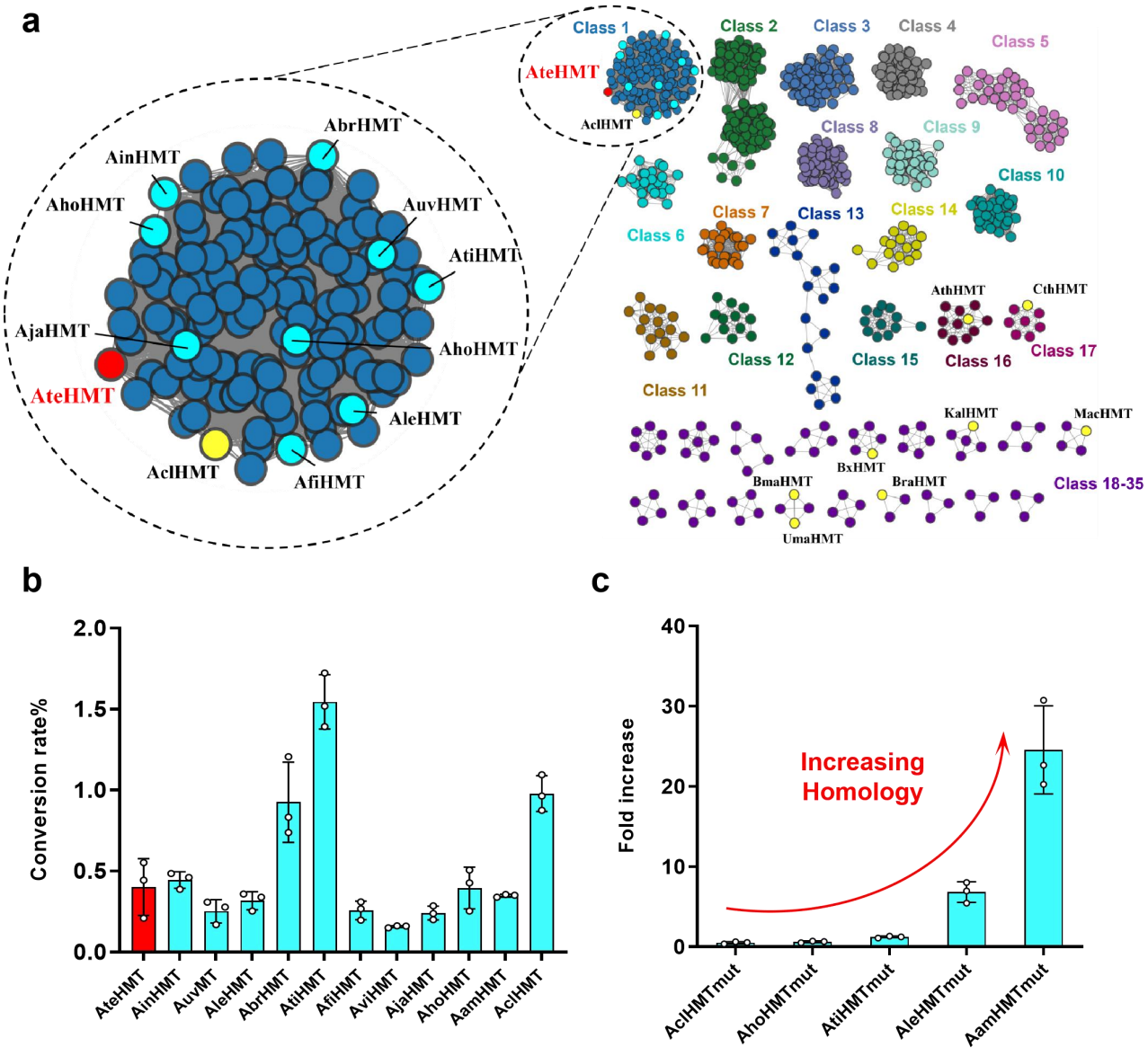

Fig.4 Explorination and engineering of *Ate*HMT family members. a, Sequence similarity network (SSN) of 1,000 *Ate*HMT homologs and 8 reported HMTs. Representative proteins selected for mutagenesis are in bright blue; reported HMTs are in bright yellow. **b,** Catalytic activity of wild-type representatives toward **1a** (conversion rate). **c,** Fold enhancement of mutants relative to their respective wild-types.

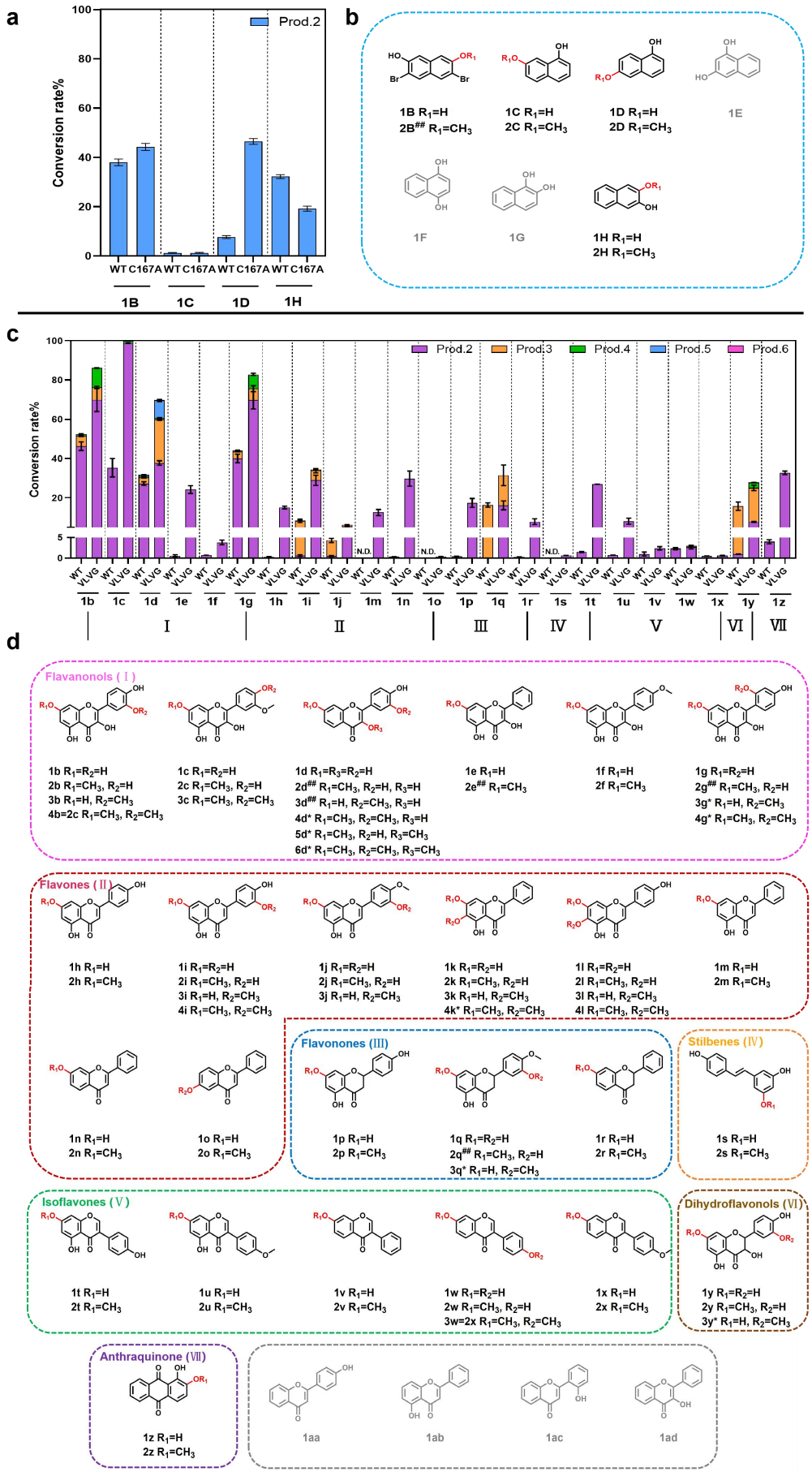

Fig.5 Exploration of substrate scope with *Ate*HMT variants. a, Methylation conversion of dihydroxynaphthalenes by *Ate*HMT-WT and *Ate*HMT-C167A. **b,** Structures of dihydroxynaphthalene substrates and corresponding methylated products. **c,** Methylation conversion of flavonoids by *Ate*HMT-WT and *Ate*HMT-VLVG. **d,** Structures of flavonoid substrates and corresponding methylated products. Reactions were performed with 2 mM methyl acceptor, 2 mM SAH, and 5/15 mM MeI, using whole cells at

OD_{600} of 80/120 in 300 µL 100 mM KPi buffer (pH 8.0) with 6/15% (v/v) DMSO for 24 h. Products were characterized by HRMS and NMR (##) or inferred from MS (*). Relative activities are mean ± SD of three independent replicates (n = 3), and conversion was determined from HPLC peak areas.

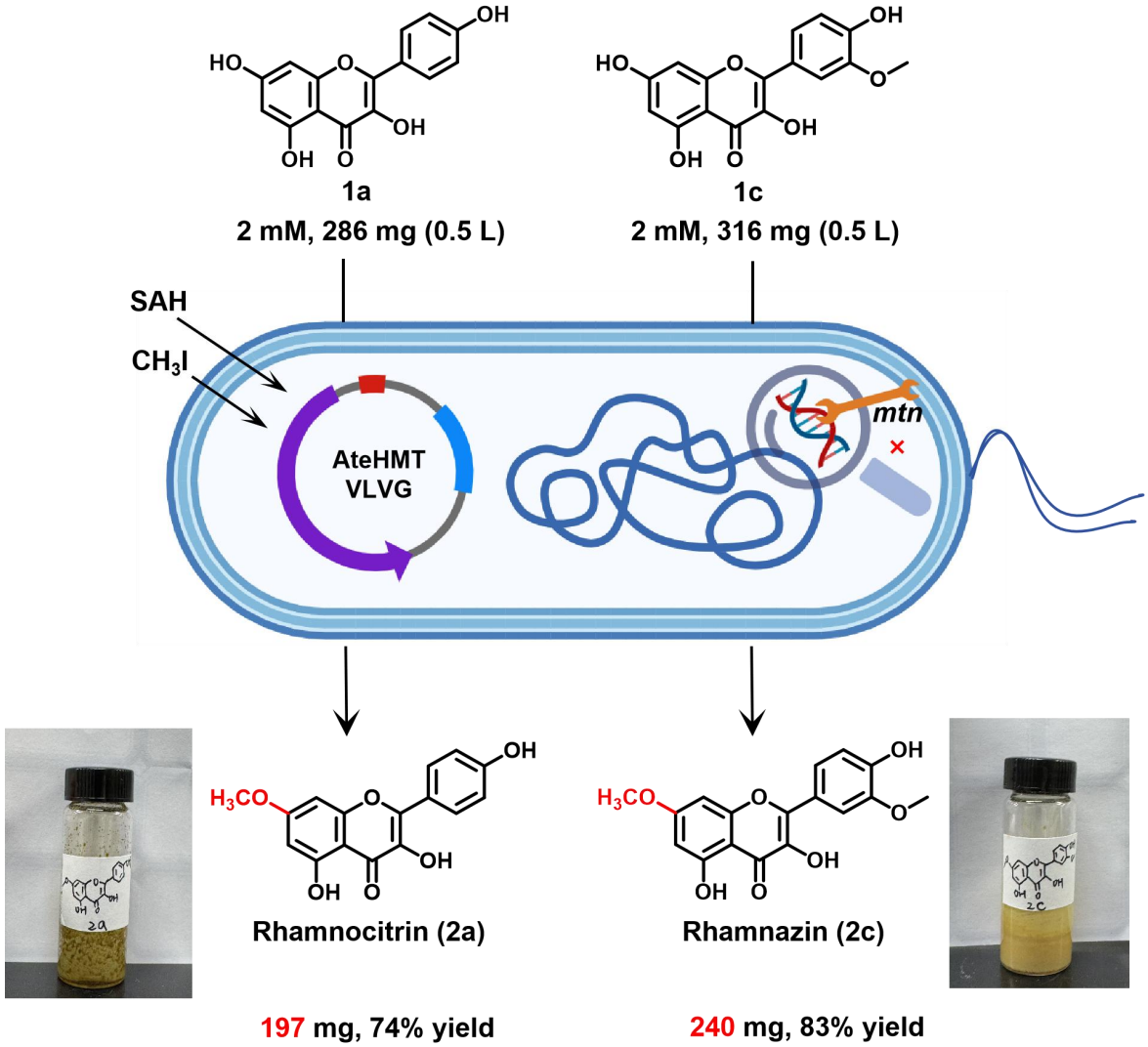

Fig.6 Preparative-scale methylation using engineered *E. coli* chassis harboring *Ate*HMT-VLVG. Gram-scale synthesis of methylated products using *E. coli* (△*mtn*::*Ate*HMT-VLVG) lysates. Cells were resuspended in 100 mM KPi buffer (pH 8.0) with 15% (v/v) DMSO and 0.1% (v/v) MeI, OD_{600} = 120, and lysed. Substrates **1a** and **1c** (2 mM each) with equimolar SAH were added to 0.5 L reaction volume, and bioconversions were performed at 30 °C, 400 rpm for 24 h.

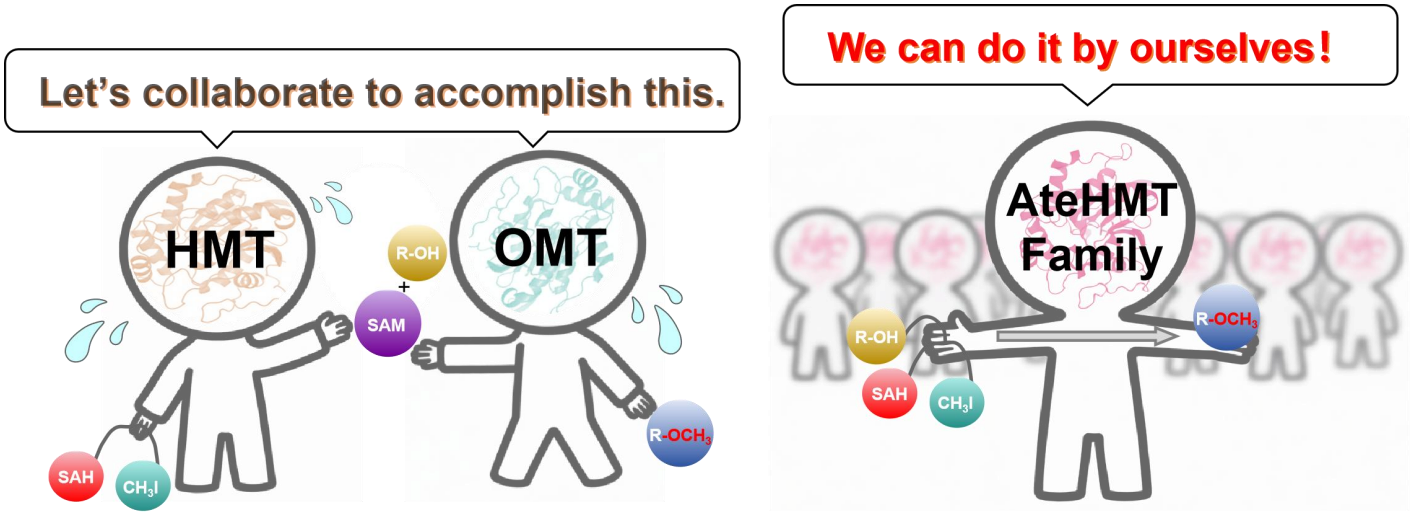

×	Low substrate mass transfer efficiency	✓	Excellent substrate mass transfer efficiency
×	Tedious operation procedures	✓	Simple and efficient operation procedures
×	High production cost	✓	Outstanding atom economy

Table of Contents

METHODS

Reagents and instruments

All chemical reagents were purchased from Aladdin, Macklin Biochemical, Meryer (Shanghai) Chemical Technology Co., 9ding Chemistry, Bide Pharm Tech, Shanghai Yuan Ye Biotechnology Co., or Sangon Biotech (Shanghai, China) unless otherwise stated. The KOD One TM PCR master Mix polymerase was obtained from Toyobo Ideas & Chemistry. *Dpn*I was purchased from Abclonal Technology. The ClonExpress MultiS One-Step Cloning Kit was obtained from Vazyme Biotech. Primer synthesis and DNA sequencing were conducted at Sangon Biotech Company (Shanghai, China). Micro-spectrophotometer (Allsheng, Nano-300), ultrasonic homogenizer with noise isolating chamber (SCIENTZ-IID), freeze drier (SCIENTZ-10ND), centrifuge (Thermo Fisher, (Sorvall ST 16R) and PICO 17), PCR Amplifier (BIO-RAD, T100^{TM} Thermal Cycler), mini shaker (Allsheng, MSC-100), shaker (Minquan, MQD-BIR). Shimadzu Nexis LC 20AT equipped with an electrospray ionization (ESI) source was used for the measurement of substrates, products and partial product standard. High resolution mass spectrometry (HRMS) detection was performed by X500R QTOF from AB SCIEX. Partial methylation products were isolated and purified by semi-preparative HPLC on an LC-8A instrument (Shimadzu). Products were characterized by ^{1}HNMR and ^{13}C NMR in DMSO-d_6 on AV2 500MHz Bruker spectrometer. Chemical shifts (δ) were given in ppm and coupling constants (*J*) were given in hertz (Hz).

Heterogonous expression and purification of HMTs

All HMTs DNA sequence were synthesized by GENEWIZ(China), and then inserted into the *Nde*I-*Xho*I site of pET28a. The recombinant plasmid pET28a-HMTs (*Ate*HMT, *Ap*HMT, *Ath*HMT, *Ana*HMT, *Pp*HMT, *Sg*HMT) were transformed into *E. coli* BL21(DE3) for heterologous expression. *E. coli* cells were cultured (5 mL) overnight in Luria-Bertani (LB) medium containing 50 μg/mL kanamycin at 37 °C with shaking (220 rpm). Subsequently, 1% seeding cultures were transferred into 500 mL TB-medium containing 50 μg/mL of kanamycin and grown at 37 °C and 220 rpm in 2 L shake flasks. After

the OD_{600} reached 0.8-1.0, the expression of recombinant *Ate*HMT were induced with 0.25 mM IPTG at 18 °C, 220 rpm for 16 h. The cells were harvested by centrifugation at 6,438 g for 3 min at 4 °C and then resuspended in 100 mM Kpi buffer (pH 8.0). After cell rupture by sonication in ice bath, the cell debris was removed by centrifugation at 15,480 g and 4 °C for 1 h. The soluble fraction was passed through a 0.45 μm syringe filter. The supernatant was applied to an ÄKTA avant 25 system equipped with a 5-mL HisTrap™ HP column following the manufacturer's instructions, using a linear gradient of 20-500 mM imidazole in 100 mM Kpi buffer pH 8.0 (Fig. S7).

Construction and screening of *Ate*HMT mutant libraries

All strains, plasmids, and primers used in this study are listed in Tables S2 and S3. PCR assays (Tab. S4) were conducted with KOD One™ PCR master Mix. Following sequence verification, the recombinant plasmids were transformed into *E. coli* BL21 (DE3) for heterologous protein expression, as described above. Single-site saturation mutagenesis (SSM) and iterative saturation mutagenesis (ISM) was performed using primers containing NNK codons at targeted sites. To ensure adequate library coverage, 92 colonies were screened per mutagenized site. Colonies were cultured in 96-deep-well plates containing 0.3 mL LB medium supplemented with 50 μg/mL kanamycin at 37 °C overnight. Subsequently, 0.7 mL TB medium containing 50 μg/mL kanamycin and 0.25 mM IPTG was added, and cultures were incubated at 18 °C for 16 h. Cells were harvested and resuspended in 0.3 mL reaction buffer (1 mM substrate **1A** or **1a**, 1 mM SAH, 15 mM MeI, 100 mM Kpi buffer, pH 7.0) and incubated at 30 °C for 24 h with shaking. Reactions were quenched by the addition of 0.9 mL methanol. Relative activity was determined by whole-cell biotransformation in a total volume of 2 mL reaction buffer (1 mM substrate **1A** or **1a**, 1 mM SAH, 15 mM MeI, 100 mM Kpi buffer, pH 7.0) at 30 °C for 24 h, using the wild-type enzyme as a control. Samples were centrifuged at 12,000 g for 15 min and analyzed by HPLC/UV using a GL Sciences InertSustain AQ C18 column (4.6 × 250 mm, 5 μm) at a flow rate of 0.8 mL/min and column temperature of 30 °C. The gradient elution programs are detailed in Table S5.

638 **Reaction condition optimization**

639 All the optimization reactions were conducted in triplicate on an analytical scale (200 μL) with 10 μM
640 enzyme, using SAH and MeI as donors and substrate **1A** or **1a** as the acceptor. To determine the optimal
641 reaction temperature, reactions were conducted at various temperatures (20 °C, 25 °C, 30 °C, 37 °C, 42 °C,
642 50 °C) for 24 hours. Both the mutant *Ate*HMT-C167A and *Ate*HMT-VLVG exhibited the highest
643 transformation rates under 30 °C reaction conditions. To evaluate the effect of the co-solvent DMSO,
644 reactions were carried out under optimized conditions with varying DMSO concentrations (3%, 6%, 9%,
645 12%, 15%, and 20% v/v). The catalytic activity of the *Ate*HMT-C167A peaked at a DMSO addition of 6%.
646 In contrast, for substrate **1a** with poor water solubility, the *Ate*HMT-VLVG exhibited higher DMSO
647 tolerance, and its catalytic efficiency reached the optimum at a DMSO addition of 15%. To study the
648 optimal pH, the enzymatic reaction was performed in various reaction buffers with pH values in the range of
649 6.0 – 8.5 (phosphate buffer) at 30 °C. Both mutants exhibited an optimal reaction pH of 8.0. Given that
650 phosphate buffer was used in the experiments and that this buffer is incompatible with metal ions, further
651 optimization of the metal ion dosage in the reaction system was not performed. We also optimized the
652 dosage ratio of SAH to acceptor substrates (**1A** and/or **1a**) across a gradient of values (SAH/acceptor
653 substrates = 0.02, 0.1, 0.2, 1, 2), and the optimal ratio was ultimately determined to be 1:1. Reactions were
654 quenched by the addition of 0.9 mL methanol, and supernatants were analyzed by analytical HPLC as
655 described previously (Tab. S5 and Supplementary Fig. S4).

656 **Determination of kinetic parameters**

657 Kinetic Study on the Stepwise Reactions of *Ate*HMT-WT, *Ate*HMT-C167A and *Ate*HMT-VLVG.

658 Step 1 (Methyl Donor Regeneration): Enzymatic assays were performed in a final volume of 200 μL at
659 30 °C for 10 min, containing 100 mM Kpi buffer (pH 8.0), 5 μM enzyme, gradient concentrations of SAH
660 (0–15 mM for *Ate*HMT-C167A and 0–8 mM for *Ate*HMT-VLVG), and MeI at a dosage 15-fold that of
661 SAH. For reaction termination, 600 μL of methanol was added to the *Ate*HMT-VLVG reaction system,

whereas 200 μL of methanol was added to the *Ate*HMT-C167A system; both mixtures were then centrifuged at 13,800 × g for 15 min.

Step 2 (Substrate Methylation Modification): For *Ate*HMT-C167A , enzymatic assays were performed in a final volume of 200 μL at 30 °C for 10 min, containing 100 mM Kpi buffer (pH 8.0), 30 μM enzyme, containing 100 mM Kpi buffer (pH 8.0), 30 μM enzyme, 2 mM saturated SAM, and varying concentrations of **1A** (0.1-1 mM). For *Ate*HMT-VLVG , enzymatic assays were performed in a final volume of 200 μL at 30 °C for 10 min, containing 100 mM Kpi buffer (pH 8.0), 10 μM enzyme, containing 100 mM Kpi buffer (pH 8.0), 30 μM enzyme, 2 mM saturated SAM, and varying concentrations of **1a** (0.01-1 mM).

Supernatants were analyzed by HPLC as described above. All experiments were performed in triplicate. The Michaelis–Menten constant (K_m) were determined from non-linear regression fitting, and the turnover number (k_{cat}) were calculated.

To determine the TON of the reactions of substrates **1A** and **1a**, 2 mM substrate was mixed with the purified enzyme 10 μM in 100 mM Kpi buffer (pH 8.0). The total reaction system was 200 μL. which was incubated at 30 °C, 1200 rpm for at least 24 h. The formation of products was determined by HPLC and the TON was calculated according to the formula TON = $[P]_{formation}$ / [E].

Protein expression and purification for crystallization screenings

Genes encoding *Ate*HMT-WT/C167A/VLVG were cloned into a modified pRSF-Duet vector, preceded by a His_6-SUMO tag, respectively. The fusion proteins were over-expressed in *E. coli* BL21(DE3) cells, which were induced by addition of 0.4 mM IPTG at an OD_{600} of 0.8-1.0 and then grown at 18 ℃ for 16 h. The cells were harvested and lysed in a buffer consisting of 25 mM Tris-HCl (pH 8.0), 1 M NaCl, 25 mM imidazole, 0.5 mM β-ME and 1 mM PMSF. The fusion proteins were first purified using a Ni-NTA column and eluted with 25 mM Tris-HCl (pH 8.0), 1 M NaCl and 250 mM imidazole. The His_6-SUMO tag was cleaved by ULP1 and romved a second Ni-NTA column. Tag-free proteins were further fractioned by size exclusion chromatography (Superdex 75, GE Healthcare) and finally stored in 25 mM Tris-HCl (pH 8.0),

300 mM NaCl, and 5% glycerol at -80 °C.

Protein crystallization and structure determination

The crystals were obtained using the hanging drop vapor diffusion method. For complex of *Ate*HMT-WT/C167A with SAH and/**1A**, the proteins (10 mg/ml) were were incubated SAH and/or **1A** at a ratio of 1:5:30 for 2h at 30℃. The crystals were grown in a reservoir solution consisting of 0.1 M sodium citrate tribasic dihydrate (pH 5.6), 25% v/v 2-propanol, and 25% w/v PEG 4000 at 20℃. The crystals of *Ate*HMT-WT-SAH and *Ate*HMT-C167A-SAH were soaked with iodomethane at supplemented into the reservoir solution to a final concerntation of 10 mM. The *Ate*HMT-VLVG protein (15 mg/ml) was first incubated with SAH and **1a** at a ratio of 1:5:30 for 1h at 30℃ before crysallization. The crystals were grown using a reservoir solution consisting of 0.1 M sodium citrate tribasic dihydrate (pH 6.0), 0.2 M ammonium acetate, and 30% PEG 4000.

The crystals were flash-frozen by immersion into a cryo-protectant containing the crystallization solution supplemented with 20-25% (v/v) glycerol, followed by rapid transfer into liquid nitrogen. The crystal data were collected at BL19U1 beamlines of the National Facility for Protein Science in Shanghai processed by HKL3000 package[48]. The structures were determined by molecular replacement using PHASER[49] in Phenix. A mode of *Ate*HMT generated by alphafold2 was used as the search model. Iterative cycles of model building and refinement were performed in COOT[50] and Phenix[51]. The data collection and refinement statistics are summarized in Table S10.

Molecular Docking

The structure of *Ate*HMT-WT-SAH-**1A** and *Ate*HMT-VLVG-SAH-**1a** were prepared using the Protein Preparation Wizard module in Schrödinger[52]. All crystallographic water molecules were removed, polar hydrogens were added and hydrogen bonds were optimized. Using the Receptor Grid Generation tool in Glide software[53], the receptor grid for molecular docking was generated at the center of the binding site of the original ligand. The 3D structures of compounds (**1i** and **1z**) were constructed using the LigPrep module,

and the possible ionization states of **1i** and **1z** were generated under conditions of pH 8.0 ± 2.0, ensuring that all relevant protonated forms were covered. Each structure was subjected to energy minimization using the OPLS4 force field[54]. Conformational ensembles were then docked into the ligand (**1A** and **1a**) binding sites using the Glide module with standard precision (SP) mode[53]. The best docking pose for **1i**/**1z** was selected based on the GlideScore and visual inspection of the binding mode.

Construction and characterization of other HMTs mutants

Using *Ate*HMT as a template to perform a BLAST search in NCBI, a total of 1,000 sequences were selected, and after SSN analysis, 10 homologous enzymes with varying degrees of homology within the same enzyme family were identified: *Aam*HMT (*Aspergillus ambiguus*, 89.36%), *Aho*HMT (*Aspergillus homomorphus* CBS 101889, 77.94%), *Abr*HMT (*Aspergillus brunneoviolaceus* CBS 621.78, 79.93%), *Ale*HMT (*Aspergillus aculeatus* ATCC 16872, 78.85%), *Ati*HMT (*Aspergillus aculeatinus* CBS 121060, 78.49%), *Afi*HMT (*Aspergillus fijiensis* CBS 313.89, 79.20%), *Auv*HMT (*Aspergillus uvarum* CBS 121591, 76.87%), *Ain*HMT (*Aspergillus indologenus* CBS 114.80, 76.51%), *Aja*HMT (*Aspergillus japonicus* CBS 114.51, 76.16%), *Avi*HMT (*Aspergillus violaceofuscus* CBS 115571 , 75.80%). Above all DNA sequences were synthesized by Sangon Biotech Co., Ltd. (Shanghai, China). Ltd, and then inserted into the NdeI-XhoI site of pET28a. The recombinant plasmid pET28a-*Aam*HMT, pET28a-*Aho*HMT, pET28a-*Abr*HMT, pET28a-*Ale*HMT, pET28a-*Ati*HMT, pET28a-*Afi*HMT, pET28a-*Auv*HMT, pET28a-*Ain*HMT, pET28a-*Aja*HMT and pET28a-*Avi*HMT were transformed into *E. coli* BL21(DE3) for heterologous expression. *E. coli* cells were cultured (5 mL) overnight in Luria-Bertani (LB) medium containing 50 μg/mL kanamycin at 37 °C with shaking (220 rpm). Subsequently, 1% seeding cultures were transferred into 500 mL TB-medium containing 50 μg/mL of kanamycin and grown at 37 °C and 220 rpm in 2 L shake flasks. After the OD_{600} reached 0.8-1.0, the expression of recombinant *Aam*HMT, *Aho*HMT, *Abr*HMT, *Ale*HMT, *Ati*HMT, *Afi*HMT, *Auv*HMT, *Ain*HMT, *Aja*HMT and *Avi*HMT were induced with 0.25 mM IPTG at 18 °C, 220 rpm for 16 h. Engineered mutants of other HMTs were constructed by PCR using KOD One™ PCR

Master Mix polymerase. The whole-cell reaction assay was performed in a final volume of 0.3 mL containing 1 mM substrate **1a**, 1 mM SAH, 15 mM MeI, 100 mM Kpi buffer, pH 8.0 , 15% (v/v) DMSO, and enzymes at an OD_{600} of 40. Reactions were carried out at 30 °C for 24 h and terminated by the addition of 0.9 mL methanol. The mixtures were then centrifuged at 13,800 g for 15 min, and the supernatants were analyzed by HPLC. All experiments were performed in triplicate (n = 3).

Genetic Operation

The *mtn* gene, which is responsible for SAH degradation, was deleted via the CRISPR/Cas9 gene-editing system. The plasmid pRedCas9 containing the Cas9 protein and plasmid with gRNA were transferred into *E. coli* BL21(DE3) competent cell, and the cells were incubated at 30 °C. Then, the cultures were transferred into fresh LB medium with a 0.20 g/L arabinose when needed.

Preparation of *E. coli* whole cell catalyst harboring *Ate*HMT mutants

After protein expression, the cells were harvested by centrifugation at 6438 g for 2 min at 4 °C, then resuspended in binding buffer (100 mM Kpi buffer, pH 8.0) at OD_{600} =120, complete cell lysis was achieved using an ultrasonic disruptor.

HPLC-ESI and HRMS-based HMTs activity assay

For the in vitro activity assay, the reaction mixture contained 2 mM SAH, 30 mM MeI, 2 mM flavonoid acceptor substrate, 15% (v/v) DMSO, the whole-cell lysate (OD_{600} = 120) or 2 mM SAH, 10 mM MeI, 2 mM naphthalene acceptor substrate, 6% (v/v) DMSO, the whole-cell lysate (OD_{600} = 60) in a total volume of 300 μL of 100 mM Kpi buffer (pH 8.0). Reactions were incubated at 30 °C for 24 h and quenched by addition of 900/300 μL methanol. After centrifugation at 13,800 g for 15 min, the supernatants were analyzed by HPLC-ESI and high-resolution mass spectrometry (HRMS). All reactions were performed in triplicate. Gradient programs used for analysis are detailed in Table S5 and Figs. S18-S42. For the substrate scope experiments, conversion rates were determined from the ratio of the product peak area to the substrate peak area in HPLC.

Product identification by NMR

Recombinant *E. coli* strains harboring pET28a-*Ate*HMT-C167A, or pET28a-*Ate*HMT-VLVG were prepared and induced as described above. After induction, the whole cells were harvested by centrifugation and washed with 100 mM Kpi buffer (pH 8.0) . The cells were then resuspended in the same buffer, and the optical density was adjusted to OD_{600} = 80/120. The reaction mixture (total volume: 50 mL in a 250 mL Erlenmeyer flask) was prepared by adding 2 mM acceptor substrate, 2 mM SAH and 10 or 30 mM MeI. Bioconversion was carried out at 30 °C with shaking for 24 h. After the reaction, the mixture was extracted with an equal volume of ethyl acetate and centrifuged at 6438 g for 10 min. The supernatant was collected and transferred to a separating funnel, where the aqueous phase was discarded, and the organic phase was retained. The solvent was removed under reduced pressure, and the resulting residue was dissolved in methanol and purified by reverse-phase semi-preparative HPLC. The purified products were dissolved in DMSO-d_6 and characterized by ^{1}H and ^{13}C NMR spectroscopy (Fig. S43-53).

48 Minor, W. *et al.* Optimal structure determination from sub-optimal diffraction data. *Protein Sci.* **31**, 259-268 (2022).
49 McCoy, A. J. *et al.* Phaser crystallographic software. *J. Appl. Crystallogr.* **40**, 658-674 (2007).
50 Emsley, P. & Cowtan, K. Coot: Model-building tools for molecular graphics. *Acta Crystallogr. D.* **60**, 2126-2132 (2004).
51 Adams, P. D. *et al.* Phenix: Building new software for automated crystallographic structure determination. *Acta Crystallogr. D.* **58**, 1948-1954 (2002).
52 Sastry, G. M., Adzhigirey, M., Day, T., Annabhimoju, R. & Sherman, W. Protein and ligand preparation: Parameters, protocols, and influence on virtual screening enrichments. *J. Comput. Aided Mol. Des.* **27**, 221-234 (2013).
53 Friesner, R. A. *et al.* Glide: A new approach for rapid, accurate docking and scoring. 1. Method and assessment of docking accuracy. *J. Med. Chem.* **47**, 1739-1749 (2004).
54 Jorgensen, W. L. & Tirado-Rives, J. The opls potential functions for proteins, energy minimizations for crystals of cyclic peptides and crambin. *J. Am. Chem. Soc.* **110**, 1657-1666 (1988).